A 16 × 16 CMOS Amperometric Microelectrode Array for Simultaneous Electrochemical Measurements

Christos Giagkoulovits, *Student Member, IEEE*, Boon Chong Cheah, Mohammed A. Al-Rawhani, Claudio Accarino, Christoph Busche, James P. Grant, and David R. S. Cumming, *Fellow, IEEE*

***Abstract*— There is a requirement for an electrochemical sensor technology capable of making multivariate measurements in environmental, healthcare, and manufacturing applications. Here, we present a new device that is highly parallelized with an excellent bandwidth. For the first time, electrochemical cross-talk for a chip-based sensor is defined and characterized. The new CMOS electrochemical sensor chip is capable of simultaneously taking multiple, independent electroanalytical measurements. The chip is structured as an electrochemical cell microarray, comprised of a microelectrode array connected to embedded self-contained potentiostats. Speed and sensitivity are essential in dynamic variable electrochemical systems. Owing to the parallel function of the system, rapid data collection is possible while maintaining an appropriately low-scan rate. By performing multiple, simultaneous cyclic voltammetry scans in each of the electrochemical cells on the chip surface, we are able to show (with a cell-to-cell pitch of 456 μm) that the signal cross-talk is only 12% between nearest neighbors in a ferrocene rich solution. The system opens up the possibility to use multiple independently controlled electrochemical sensors on a single chip for applications in DNA sensing, medical diagnostics, environmental sensing, the food industry, neuronal sensing, and drug discovery.**

***Index Terms*— Amperometric sensors, CMOS, cyclic voltammetry, electrochemical sensor, electrochemical cross-talk, microelectrodes, potentiostat.**

I. Introduction

THE electrochemical cell, first demonstrated by Volta and Banks [1], is the foundation of many chemical, biological and sensing technologies [2]. Applications include the popular point-of-care glucose sensor [3], commercial electrochemical gas sensors [4], epiretinal implants [5] and the study of electrogenic cells to further understand the most complex human organ, the brain [6]. In recent years, the microelectrode array (MEA) has risen to prominence in biomedical and environmental redox sensing owing to the low-cost possibility of making many measurements in parallel with high current densities in small volumes, and detection of electroactive species at low concentrations [7]. Despite many advances in the technology [8], numerous problems have yet to be overcome, including low data acquisition speed and poor isolation between electrochemical cells. The latter leads to high cross-talk between adjacent sensors and an inability to make many independent measurements in parallel. We describe and implement a novel complementary metal oxide semiconductor (CMOS) scalable architecture combining new electrode layouts and circuits that enable a reliable planar system of electrodes, connected to an array of potentiostats. Integrating the electrode system in CMOS offers improved signal-to-noise ratio (SNR), parallel data collection, a high-level of circuit and microelectrode integration and fast adaptable spatiotemporal multiplexing at a low unit cost [9], [10].

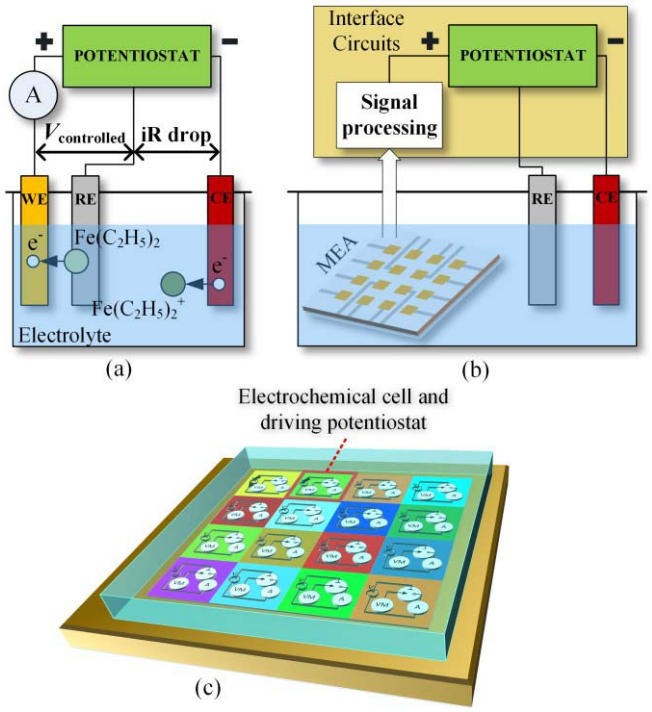

Fig. 1. Illustration of operation of (a) a three-electrode electrochemical cell operated by a potentiostat using ferrocene ($Fe(C_5H_5)_2$) as an analyte. (b) A MEA in solution and its interface. (c) Conceptual illustration of a multivoltammetric electrochemical cell microarray (ECM).

Fig. 1(a) shows a traditional three-electrode electrochemical cell. The cell consists of a working, counter and reference

Manuscript received July 21, 2017; revised October 24, 2017 and December 31, 2017; accepted January 2, 2018. Date of publication February 6, 2018; date of current version August 3, 2018. This work was supported by the Engineering and Physical Sciences Research Council under Grant EP/K021966/1. This paper was recommended by Associate Editor M. Onabajo. *(Corresponding author: Christos Giagkoulovits.)*

C. Giagkoulovits, B. C. Cheah, M. A. Al-Rawhani, C. Accarino, J. P. Grant, and D. R. S. Cumming are with the Microsystems Technology Group, School of Engineering, University of Glasgow, Glasgow G12 8LT, U.K. (e-mail: c.giagkoulovits.1@research.gla.ac.uk; boonchong.cheah@glasgow.ac.uk; mohammed.al-rawhani@glasgow.ac.uk; c.accarino.1@research.gla.ac.uk; james.grant@glasgow.ac.uk; david.cumming.2@glasgow.ac.uk).

C. Busche is with the Westchem, School of Chemistry, University of Glasgow, Glasgow G12 8QQ, U.K. (e-mail: christoph.busche@glasgow.ac.uk).

Color versions of one or more of the figures in this paper are available online at http://ieeexplore.ieee.org.

Digital Object Identifier 10.1109/TCSI.2018.2794502

electrode (WE, CE and RE respectively). A redox reaction is developed by the application of an electric potential between the WE and CE in the electrolyte and the resulting current is measured on the WE. The potential is adjusted so that $V_{\text{controlled}} = V_{\text{WE}} - V_{\text{RE}}$ (set by a function generator) and the RE corrects for the Ohmic (iR) drop that occurs in the electrolyte, electrodes and circuit impedances. By controlling the system using a potentiostat, a range of electrochemical measurements, such as cyclic voltammetry, become possible [11]. Furthermore, potentiostats can also be used to control electrodes in an MEA, as shown in Fig. 1(b). By doing so, electrodes can be miniaturized thus enabling multiple measurements to be made on a single chip. In this work, we present an electrochemical cell microarray (ECM) system that demonstrates a 4×4 array of wholly independent electrochemical cells each driven by their own potentiostat, as shown in Fig. 1(c). To realize the ECM, a new electrode layout and circuit design was developed.

Electrode layouts are typically designed by evaluating their potential and current density distributions using electrochemical simulations. In previous studies, using MEAs for electrochemical applications, the use of guard rings has been explored to improve the isolation between independently controlled electrodes [5], [12], [13]. Improved isolation was shown experimentally and by simulation. Planar diffusion of the analyte species led to a "shielding" effect that degraded the electroanalytical performance, as a consequence of overlapping Nernst radial diffusion layers. A 40 % decrease of the expected current of a central WE surrounded by other active WEs has been reported [14]. This is regarded as chemical cross-talk [15]. It has been shown that the formation of a planar diffusion layer can be prevented by fabricating the CE in a guard ring structure surrounding the WE [16]. The electrical cross-talk in MEAs occurs because of electrical coupling through the solution or the integrated electronic elements, it has been shown to vary from below 0.1 % to more than 10 % [17]. Electrical cross-talk has also been observed at neighboring microelectrodes operated at different potentials [18]. There remains a requirement to create arrays capable of multiple concurrent electrochemical experiments that is not possible using the structures outlined above. The main challenge is to minimize both chemical and electrical cross-talk between adjacent electrochemical cells – a problem that has been noted but not addressed to date [19], [20]. Experimental and simulation studies of a new coaxial three-electrode geometry and a unified electrochemical cross-talk figure of merit are presented.

In order to verify our new electrode system, we designed and implemented an integrated circuit. Although cross-talk has not previously been quantified, fast scan cyclic voltammetry (FSCV) along with other electrochemical techniques have been explored using separate, non-integrated, microfabricated electrodes [20], [21]. Previous work on CMOS has shown that electrodes can be set at various offset voltages by a single integrated potentiostat [22]. In an attempt to overcome the current supply limitation of using a single potentiostat it was shown that several potentiostats could be integrated and used simultaneously to perform a single measurement [23]. In this paper, a CMOS ECM is presented, comprised of fully differential potentiostats [24], capable of regulating inter-cell potential interference. Our device is capable of performing independent concurrent analyte-tailored analysis by different types of electroanalytical techniques on every cell simultaneously, including constant potential amperometry and square wave voltammetry. The high bandwidth potentiostats allow for FSCV to be used at high scan rates and different potential settings can be applied per electrochemical cell. Au bio-functionalizable electrodes were integrated to enable multiplexed DNA "probe" monolayer synthesis [25]. These features allow for the development of an electrochemical DNA microarray [23], [26] for genotyping with increased selectivity. The microarray would allow identifying a hybridized DNA "target" sequence per cell which would be tagged with redox labels, such as ferrocene and its derivatives, each with a different redox potential [27].

The way in which the system was designed to enable independent measurements, allowed for another feature to be exploited. By the use of a novel technique that allows independent control over each cell in an array, we obtained undistorted cyclic voltammograms (CVs) faster than their low scan rates (υ) would normally allow. This feature can be used for other applications that involve short-lived intermediate compounds.

This paper is organized as follows. Section II describes the electrochemical modeling and simulations that lead to an independent electrode configuration. Section III focuses on the electronic circuit design of the array and Section IV details the post-processing steps on the CMOS die. In Section V the chip is characterized and in Section VI materials, methods and experimental results that demonstrate the electrochemical cells' independence of operation are presented. In Section VII our system is compared to the state-of-the-art and in Section VIII the paper is concluded.

II. Electrochemical Cell Microelectrode Layout Simulations

In order to develop a complete circuit simulation, it was necessary to develop an electronic model for the behavior of the analyte and its interaction with the electrode layout using simulation methods fully compatible with integrated circuit computer-aided design (CAD) software (Cadence®). A suitable layout for the electrodes was investigated for an electrochemical cell array, with cells operating independently of each other. Fig. 2(a) shows a conventional pattern of electrodes, similar to the ones used in previous work [23] and Fig. 2(b) shows a coaxial structure we designed with the CE and RE surrounding the WEs. For the purposes of this simulation we used 4 WEs as a representative example. To understand the electric field and potential distribution associated with the patterns in a chemical solution we developed an equivalent circuit model using a netlist comprising of resistors and capacitors [28]. The electrical model for an electrolyte in solvent was constructed by a 3D cubic mesh of resistors, R_{el} as in [29] for a solution volume of 200 μm $\times$ 200 μm $\times$ 90 μm. In our simulation we assumed the solution to be made up of 0.1 M tetrabutylammonium hexafluorophosphate ($TBAPF_6$) in

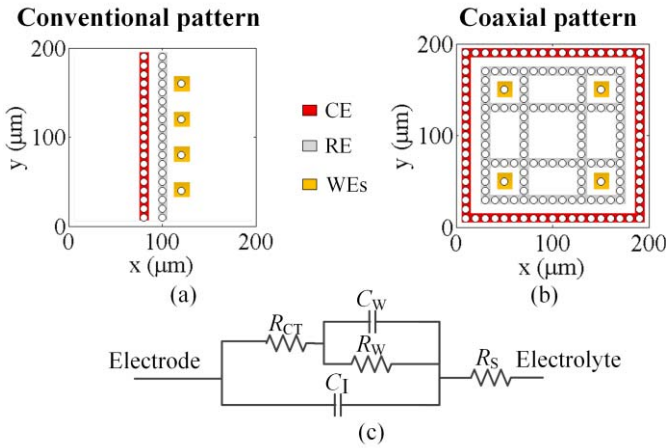

Fig. 2. Electrochemical cell electrode geometries for (a) a conventional and (b) a coaxial pattern. (c) The electrode-electrolyte interface model.

TABLE I

PARAMETERS REQUIRED FOR THE CALCULATION OF RANDLES MODEL IMPEDANCES

Parameters used for calculations	Values	Calculated Randles impedance	Values used in model
ρ	60.82 Ω·cm [30]	R_{CT}	39.1 MΩ
z	1	R_W	92.2 MΩ
U_t	26 mV @ 298K [33]	C_W	1.73 nF
k^0 [35]	6.74 m/s	C_I	10.6 fF
α [35]	0.6	R_S	26.8 kΩ
ε_r	37.50 [51]		
d_{OHP} [33], [37]	3.14 μm		
D_{Fc}	2.60 x 10^{-9} m^2/s [52]		

Impedance values were calculated for a 10 μm × 10 μm electrode area.

acetonitrile with a resistivity ρ of 60.82 Ω·cm [30]. From this $R_{el} = \rho/x$ could be determined, where x is the grid size of the cubic lattice; x in our simulations was chosen to be 10 μm, hence $R_{el} = 60.82$ kΩ. The WEs, CE and RE were modelled in a transmission line format [31] in order to take into account their geometries. They were modelled as two dimensional elements of a 10 μm × 10 μm area and represented as points in Fig. 2(a) and 2(b); WE elements were modelled as a 20 μm × 20 μm area. These points were connected together with 40 mΩ/□ resistors, which was the sheet resistance of a typical metal layer in a CMOS process, to form the shapes of electrodes. Each point was connected to the mesh using a Randles electrode-electrolyte model [32], [33] as shown in Fig. 2(c).

To determine the component values of the Randles model the addition of 20 mM of ferrocene ($Fe(C_5H_5)_2$) to the solvent was assumed. R_{CT} is the charge transfer resistance calculated from a low field approximation of the Butler-Volmer equation for well stirred solutions [33]:

$$i = i_0 \frac{z\eta}{U_t} \tag{1}$$

where i_0 is the equilibrium exchange current, z is the number of exchanged electrons, η is the overpotential and $U_t = RT/F$ is the thermal potential, where R is the gas constant, T is the temperature and F is Faraday's constant. For low fields, (1) can be translated into Ohms law $R_{CT} = U_t/i_0 z$. i_0 was calculated by the equation $i_0 = AFk^0 C_R^{\alpha} C_O^{1-\alpha}$ [34], where A is the electrode area, C_R and C_O are concentrations of the reduced and oxidized form of the analyte respectively, α is the transfer coefficient and k^0 is the standard rate constant. k^0 was calculated by experimental observations [35], using a CHI600D commercial potentiostat from CH Instruments. R_W and C_W is the Warburg impedance for non-Faradaic processes. An important parameter for its calculation is ferrocene's diffusion coefficient, D_{Fc} [36]. C_I is the combination of Helmholtz and Gouy-Chapman capacitance describing the electrical double layer calculated by the Stern-Gouy-Chapman model [36]. Parameters required to calculate C_I include the dielectric constant (ε_r) of acetonitrile, and the electrical double layer thickness (d_{OHP}) [33], [37]. R_S is called a spreading resistance and represents the current spreading from an electrode of known size and geometry; for rectangular electrodes $R_S = \rho/\pi l \times \ln(4l/w)$, where w, l are the width and length of the electrode respectively [36]. The parameter values specific to the solution composition assumption and the model impedances values are all summarized in Table I.

Having developed netlists representing electrode layouts in a chemical solution, we used them in an integrated circuit simulation (Cadence®) of a fully differential potentiostat design [24]. A dc response was recorded as a snapshot. The potential distribution in each cell was plotted against its V_{WE}, since $V_{controlled} = -(V_{RE} - V_{WE})$. Owing to the differential nature of the potentiostats V_{WE} was adjusted at a different level for each electrochemical cell. The simulation ignored effects of mass transfer and electro-osmosis.

The simulation results for the electric field, the potential distribution and the current density are presented in Fig. 3. We used a coaxial geometry to isolate the WEs inside their respective cells. As it can be observed in Fig. 3 (a) and (b), a close WE pitch is responsible for overlapping electric field intensity areas, which has been identified as a source of electrical cross-talk [13]. The electric field is also associated with analyte diffusion [11], the separation of radial diffusion layers among the WEs is essential for high mass transfer behavior on microelectrodes [15]. The coaxial geometry was designed to meet those requirements.

Concerning the potential distribution, the simulations showed that a potentiostat would establish a defined potential around the RE. The potential of the CE was adjusted to a higher value than V_{RE} to compensate for the iR drop, as evident in Fig. 3(c-f). The effect of the electrode layout is prominent in the electric field and current density, which are related by $\vec{J} = \vec{E}/\rho$. Whereas for the conventional geometry the current was estimated to flow from the CE to the WEs in a cylindrical shape, shown in Fig. 3(c) and (e), an inwards cycling "fountain" flow would occur at the coaxial geometry, as shown in Fig. 3(d) and (f). Moreover, the coaxial layout benefits from an equipotential area, which would develop in the vicinity of the RE and be guarded by the surrounding CE, as displayed in Fig. 3(d). Although the use of CE rings around each WE could improve intra-cell isolation, it was not done in order to minimize capacitive coupling caused by interconnections between CE rings.

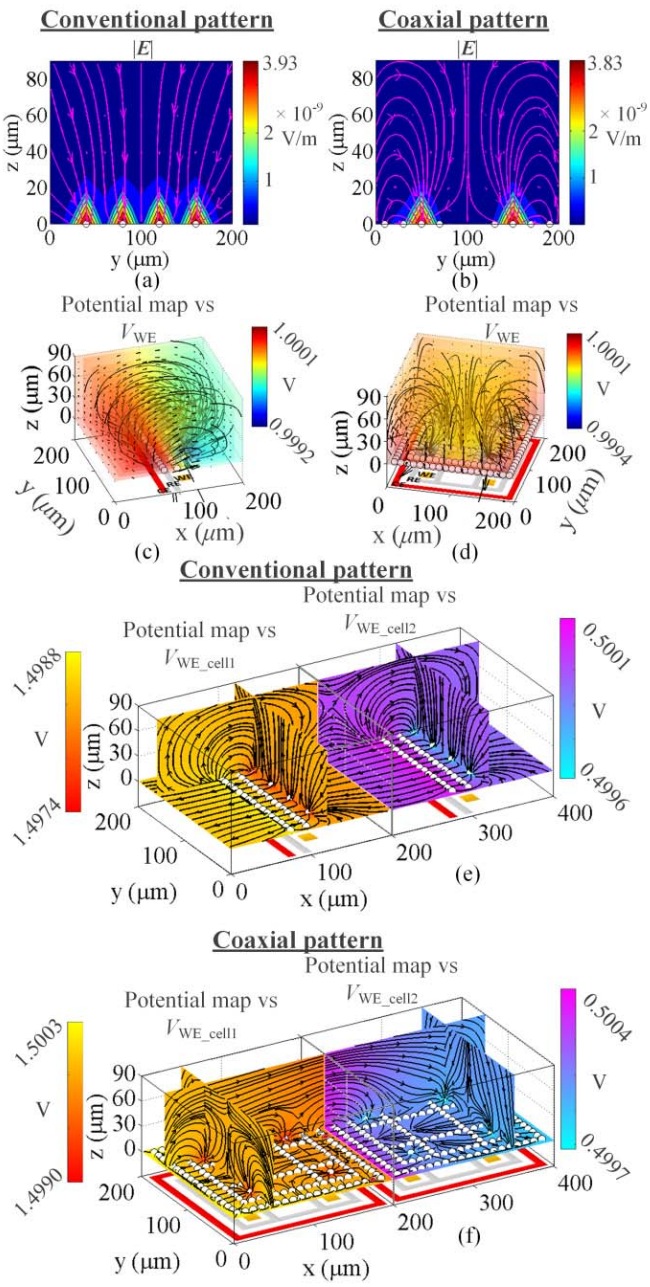

Fig. 3. A YZ slice of the electric field intensity at the WEs of (a) a conventional and (b) a coaxial geometry. 3D Potential distribution against V_{WE} and current density vector of (c) a conventional and (d) a coaxial geometry for $V_{controlled} = -1$ V. Slices of potential distribution and current density vector for simultaneously operated adjacent electrochemical cells in (e) a conventional and (f) a coaxial geometry against every cell's V_{WE}. The cells were set at $V_{controlled\_cell1} = -1.5$ V & $V_{controlled\_cell2} = -0.5$ V respectively.

Cells were simulated in pairs of 4 WEs set at different potential levels. The simple design of the conventional pattern resulted in poor regulation of the potential distribution, as observed on the left cell of Fig. 3(e). The source of the problem was an inter-cell leakage current originating from the CE of the neighboring cell. Conversely a lower leakage current, mainly between CEs, was observed in simulations among coaxially patterned cells, as shown in Fig. 3(f). The coaxial arrangement regulated the CE potential accordingly to maintain a stable intra-cell current flow to the WEs and limit inter-cell mass transfer.

By simulating the behavior of the entire system, including electronics and electrode kinetics, we gained a unique insight into the operation of the device. The coaxial electrode pattern exhibited promising results for its use in an ECM, especially when combined with a fully differential potentiostat in a design explained in the next section.

III. Independent Electrochemical Cell Microelectrode Array CMOS Design

The ECM design consists of 4×4 electrochemical cells arranged in a 456 μm pitch. Electrodes were integrated together with electronics on the same CMOS chip to enable localized control. Each cell contains a 16 WE sub-array and a fully differential potentiostat [24] driven by separate differential input signals. The sub-array WEs were arranged in a 114 μm pitch coaxial geometry surrounded by a CE and a RE. The geometry was based on our layout simulations and it was expected to follow the behavior of the simulated 4 WE geometry (Fig. 4(a)).

The integrated potentiostat is comprised of OP1, a two-stage high gain fully differential folded cascode control opamp with a common mode feedback loop (CMFB) [38] and 2 unity gain amplifiers (OP2 and OP3), as shown in Fig. 4(b). The fully differential control opamp, shown in Fig. 5, allows for common mode noise suppression and individual regulation of the CE and WEs potentials. This feature is critical for applying independent multiple voltammetric electrochemical experiments, as well as increasing the output voltage swing of low-voltage CMOS circuits towards a broader analyte selection range.

Using our simulation netlist, the control opamp was designed to have a unity gain bandwidth of 3.3 MHz with a phase margin of 110° since it was Miller compensated, and a DC gain of 77 dB. To achieve these specifications the power dissipation was 940 μW. A circuit of high sheet resistance integrated polysilicon resistors of 500 kΩ coupled with 1 pF compensation polysilicon capacitors was used to detect the common mode signal in the CMFB. The compensation and CMFB needed in the opamp are largely responsible for the dissipation figure. Each of the unity gain amplifiers dissipated 234 μW in simulation, and exhibited a unity gain bandwidth of 29 MHz with a phase margin of 113° and a DC gain of 92 dB.

Overall the system operates as follows. A pair of input voltages, $V_{IN+}(i)$ and $V_{IN-}(i)$, are supplied externally to each potentiostat. These voltages drive the control opamp (OP1) and a feedback loop by the unity gain amplifiers (OP2 and OP3) maintains the potential difference of $V_{WE} - V_{RE}$, in each potentiostat. A redox reaction develops at the WEs which are multiplexed by WE_{EN} using a rolling shutter method. The related current is converted to the output voltage at the cell's readout resistor ($R_{I\ to\ V}$). The output voltage changes represent the degree of reduction or oxidation occurring at the WE.

Unlike the conventional readout method, where the entire applied potential waveform is required to be scanned through each WE, our WE sub-array was designed so that electrodes were multiplexed over segmented voltage levels. However,

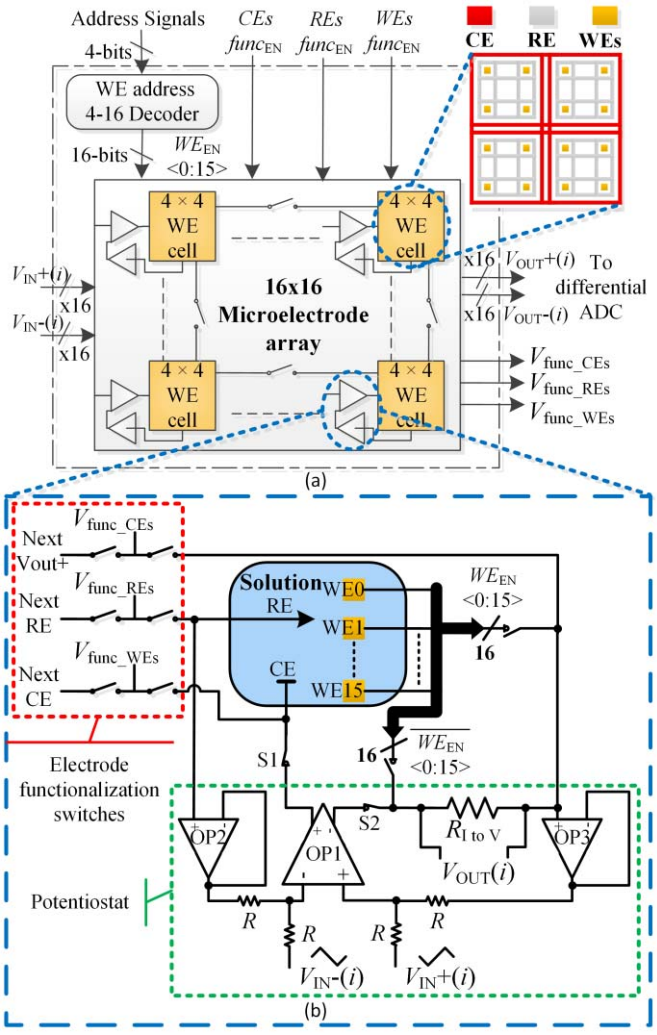

Fig. 4. (a) System overview and electrode geometry detail (b) electrochemical cell switching readout circuit, the fully differential potentiostat and functionalization switches for microelectrodes.

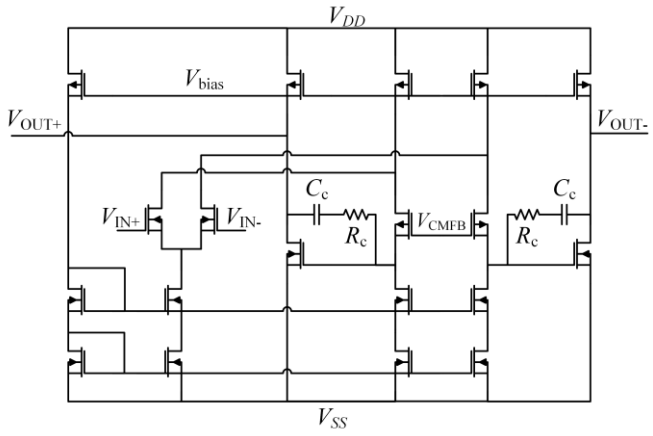

Fig. 5. The fully differential folded cascode control opamp circuit design.

multiplexing can cause voltage perturbation and as a consequence a disturbance of the analyte diffusion layer. To prevent such problems and sustain the current flow all WEs were connected to similar potentials (within a few mV). Non-addressed WEs were connected to the negative output of the control opamp by the $\overline{WE_{EN}}$ switches [16], [39], as shown in Fig. 4(b).

A novel additional feature was also added to the design to enable the chip's functionalization e.g. electrodeposition. Microelectrodes can be functionalized using a voltage potential that can be applied externally (V_{func_CEs}, V_{func_REs} and V_{func_WEs}), as shown in Fig. 4. The selection of each type of electrodes can be enabled using integrated switches (transmission gates) incorporated in each cell (*CE* $func_{EN}$, *RE* $func_{EN}$ and *WE* $func_{EN}$). To isolate the electrodes during functionalization the driving circuit is disconnected by switches (*S*1 and *S*2). When the ECM was normally operated, all $func_{EN}$ control signals were on the "off" position and V_{func} pins were connected to ground.

The system was designed in a 4-metal 350-nm CMOS process and was fabricated by ams AG through the Europractice mini@sic multi project wafer service. The array's active area is 1.814 mm × 1.814 mm.

In order to test and validate the chip, the inputs and outputs were connected to a National Instruments© PXIe interface system, which consisted of a PXIe-1073 chassis and three cards, a PXI-6723, a PXI 6704 for the analogue inputs and a PXIe-6358 with a 1.25 MS/s/channel capability that read the analogue outputs. A LabVIEW program was developed to perform electrochemical experiments and analyze the results. WEs were switched at frequencies up to 6.4 kHz with a sampling rate of 32 kS/s/channel for the analogue outputs.

In order to prepare the microelectrodes on CMOS technology so that experiments could be carried out, it was necessary to perform post-processing. This is described in Section IV.

IV. ECM Post Processing and Encapsulation

The electrodes were coated with Au since it makes them more electrochemically inert. Furthermore, Au can be readily modified e.g. with thiol chemistry for use in biosensing applications. The Al metal used by the foundry is not biocompatible and degrades easily. 800 nm of the 1 μm thick Si_3N_4 part of the passivation layer over the electrode array area was removed by etching. An overglass opening was made on the remaining passivation layer covering the Al electrodes which were designed on the top metal layer of the CMOS process and are shown in Fig. 6(a) and (c). The opening was patterned at a width 25 % smaller than the 20 μm side of the square WEs and the 11 μm wide REs and CEs using a positive photoresist (Microposit^{TM} S1818^{TM}) and etched via a reactive ion etch process of CHF_3/O_2. A pattern wider than the Al electrodes was then photolithographically defined to cover the easily corroded Al metal with a chemically resistant layer. The photoresist was pre-soaked in a tetramethylammonium hydroxide (TMAH) based developer to create an inhibition layer and form a suitable overhang [40] for metal liftoff. A stack of metal layers comprised of 20 nm Ti, 50 nm Pd and 200 nm Au was thermally evaporated and microelectrodes were formed by a liftoff process, as shown in Fig. 6(b) and (d). Pd was used as a diffusion barrier between Al and Au preventing the formation of an Al-Au intermetallic that leads to poor conductivity [41]. The exposed Al CMOS top metal layer formed a thin native Al_2O_3 layer by coming in contact

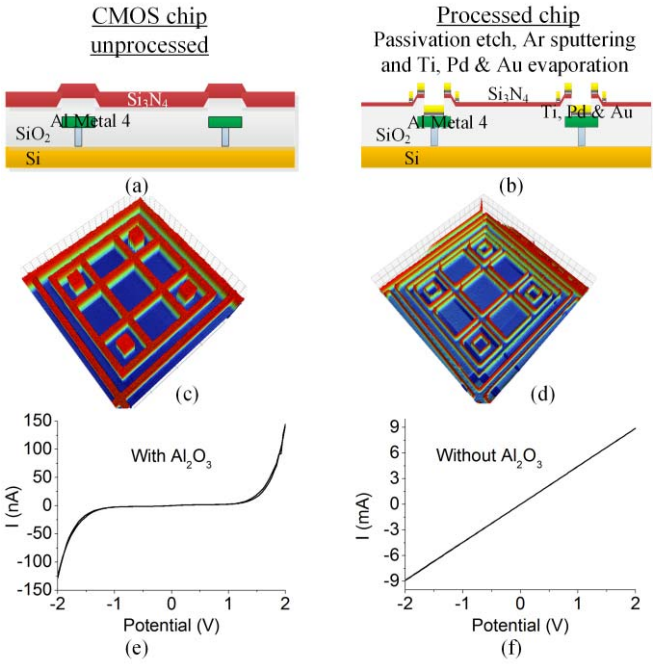

Fig. 6. Cross section of (a) the unprocessed and (b) post-processed CMOS chip. 3D surface detail of the CMOS chip measured by an optical profiler (c) before and (d) after post-processing. I-V characteristics on Al-Au dummy samples (e) with and (f) without a native Al_2O_3 layer.

with an O_2 rich environment. Tests on dummy samples, shown in Fig. 6(e-f), proved the barrier effect was caused by the oxide layer. This layer was removed by an in-situ Ar etching step before metal evaporation. In addition to the post-processing methods, an added 650 nm layer of Au was electrodeposited with a rate of 65 nm/min using the embedded functionalization method. Optical images of the post-processed chip and a close-up of the electrodes forming a single electrochemical cell are shown in Fig. 7(a).

On completion of post-processing the CMOS chip had to be encapsulated to handle liquids in a container. The die was first bonded on a ceramic PGA-144 chip carrier with an H74 epoxy from Epoxy Technology. A chemically resistive epoxy 302-3M from Epoxy Technology was used to cover and insulate the bonding wires from the solution. In order to keep the sensor array active area exposed, a polydimethylsiloxane (PDMS) cube was used to create a temporary bond and protect the active area from being covered by the epoxy until it was cured [42]. A polyethylene terephthalate glycol-modified (PETG) custom designed 3D printed test tube with a lid was then fitted using the same epoxy. The chemically resistant materials created a chamber for the chemical solutions that were electrochemically analyzed. The post-processed CMOS die in its encapsulated packaging is illustrated in Fig. 7 (b).

In order to benchmark the on-chip potentiostat design against a commercial instrument, a dummy set of microelectrodes that exactly mimicked those on the chip was prepared. The benchmark and experimental results that showcase the abilities of our ECM are presented in Sections V and VI.

V. Chip Characterization

Before any electrochemical experiment was performed, the chip was evaluated electrically to measure the maximum

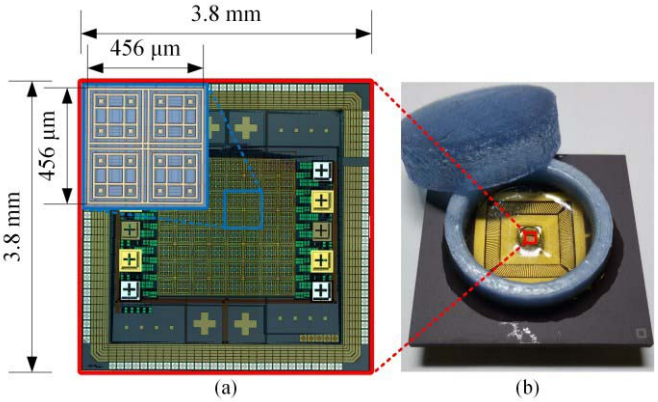

Fig. 7. (a) An optical micrograph of the post-processed CMOS chip with a detail of an electrochemical cell and (b) a picture of the same chip packaged and encapsulated.

detectable current, bandwidth, slew rate and the on-chip resistor values. The CMOS potentiostat was configured to have a unity gain by using 10 MΩ external discrete component resistors to mimic the impedance between the microelectrodes. The value of the resistors was chosen so that the current was maintained at the expected experimental levels. The amplifiers' Miller compensation resulted in a measured potentiostat bandwidth of 150 kHz, allowing FSCV at scan rates of up to 18 KV/s for a 4 V_{pp} potential scan. The potentiostat slew rate plays an important role in the correct representation of a CV and it was measured to be 1.09 V/μs. The maximum detectable current I_{max} was determined by adjusting a resistor load. Its value was found to be 13 μA using a 5 kΩ load between the RE and WE and a 50 mV input signal. To avoid measurement variations due to the tolerance of the on-chip R_{ItoV} resistors (i.e. ± 20 %), the actual value of each resistor was measured for every chip. The measured values were then used as a reference to calculate the current from voltage measurements.

VI. Electrochemical Measurements

In order to verify the ability of the platform to control and monitor redox reactions, the device had to be tested with a well-documented reference substrate. As discussed in the introduction ferrocene is an ideal candidate since it is one of the most common redox species used in electrochemical experiments for its easy to observe current peaks and its reversible properties. Ferrocene is oxidized to ferrocenium according to the reaction:

$$\mathrm{Fe\,(C_5H_5)_2} \rightleftarrows \mathrm{Fe\,(C_5H_5)_2^+} + \mathrm{e^-} \tag{2}$$

Its half-wave potential is $E_{1/2} = 415$ mV when using a $Ag^+/AgCl$ reference electrode in acetonitrile [43]. The sample solutions were prepared using 99+ % pure acetonitrile (CH_3CN) and ferrocene ($Fe(C_5H_5)_2$) with 98 % purity, both from ACROS OrganicsTM (purchased from Fischer Scientific). Tetrabutylammonium hexafluorophosphate ($TBAPF_6$) was used as the supporting electrolyte with 98 % purity from Sigma Aldrich.

The on-chip potentiostats were first benchmarked against a commercial CHI600D potentiostat from CH Instruments. To keep the measurements standardized the aforementioned

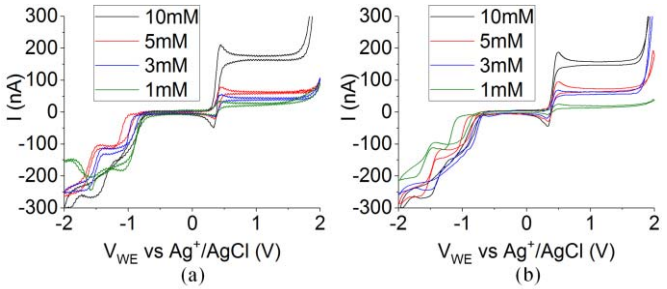

Fig. 8. Cyclic voltammograms using dummy microelectrodes operated by (a) a commercial and (b) the CMOS potentiostat.

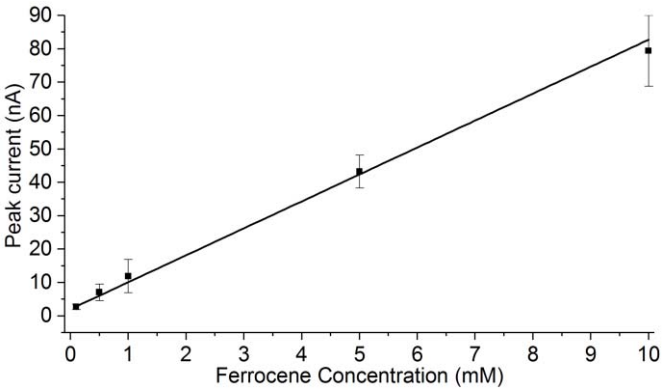

Fig. 9. Ferrocene concentration response curve for the average of all 256 WEs.

4×4 WE dummy microelectrode arrangement, described in Section IV was used with both potentiostats. A Ag^+/AgCl external RE that was made by electrolyzing a Ag wire in 3 M KCl and a Pt wire as a CE were used for the purpose of these experiments. Solutions of 1 mM, 3 mM, 5 mM and 10 mM ferrocene in acetonitrile with 0.1 M $TBAPF_6$ were prepared. Acetone and isopropanol were used to rinse and clean the microelectrodes between experiments. The CVs were run on both devices using the same settings of 2 V/s scan rate, scanned in a positive direction and considering the anodic current as positive, plotted in Fig. 8(a) and 8(b). In this experiment the signals of the ASIC were not multiplexed; only one of the chip's fully differential potentiostats was used to drive the external microelectrode setup. A smoothing filter was applied digitally after signal acquisition to the data from measurements with the chip. As expected CVs exhibited peak currents around $E_{1/2}$ (as the half-peak potential is $E_{p/2} \approx 400$ mV), ranging in magnitude proportionally to the analyte concentration. The fully differential design of the CMOS potentiostat enabled us to reach V_{WE} vs Ag^+/AgCl potentials from -2 V to 2 V despite its 3.3 V bias voltage. Peaks observed at these extreme voltages result from the oxidation and reduction of the solvent and the supporting electrolyte. The results are almost identical in both potentiostats.

After verification of the electronic components, measurements with the post-processed electrodes of the encapsulated CMOS ECM were performed. Staircase voltammetry was performed, by applying a waveform of segmented voltage levels. A common differential waveform, using the same rate as before of 2 V/s, was applied as an input of all independent cells, resulting in a uniform platform monitoring the same reaction. Each cell's WEs were multiplexed over voltage levels that had a 10 ms duration, as explained in Section IV. Two digital non-linear 1D median filters were applied to data from the output signals to remove impulse noise, originating from the NI PXIe input source. This measurement resulted in 256 concurrent independent CVs monitoring the ion activity at approximately the same points in time. Results from all electrochemical cells were averaged to minimize interference from single WEs. Concentrations of ferrocene from 100 μM to 10 mM were analyzed and their respective CVs were captured. The anodic and cathodic peak currents of all cells were averaged to demonstrate the peak current signal per concentration response, as shown in Fig. 9. A linear fit line was drawn that describes this relation. The quiescent power dissipation of the microchip was also measured using this experimental arrangement. Using a 0 V DC signal input on all cells the power dissipation was 42.9 mW, whereas on the highest detectable ferrocene concentration and an input waveform at a high scan rate $\upsilon = 8$ V/s it was 125.4 mW. In addition to the power consumption of the internal circuits there are other parameters that can affect the power dissipation such as the chemical solution composition as well as an inter-cell potential difference between CEs as a trade-off of isolation.

A. Cross-Talk

The key feature of this multichannel microelectrode array is the ability to use isolated electrochemical cells in the same solution and perform independent electrochemical techniques simultaneously on the same chip. To demonstrate this capability two experiments were carried out to evaluate cross-talk. In the first of these, the central cell, indicated by a green box in Fig. 10(a), was activated to perform a 2 V/s staircase CV. As can be seen on Fig. 10(b) there is a current detected on the WEs of the activated cell, but negligible current is observed on any of the other cells. The complementary experiment was also conducted whereby the central cell was not activated, but the potential on the neighboring cells was swept, as shown in Fig. 10(c). Fig. 10(d) shows how there is small current detected on the WEs of the inactive central cell. The solution was of the same composition as before with ferrocene at a concentration of 5 mM. The REs in this case were on-chip, fabricated with an Au interface, as explained in Section IV. Au acted as a quasi-reference electrode and is responsible for a redox potential shift to $E_{p/2} = 75$ mV. Each experiment's values from 50 cyclic voltammetry cycles were averaged and used for the cell-to-cell electrochemical cross-talk calculation, using (3):

$$\text{cross-talk} = \frac{\sum_{V_n=V_{\text{peak}}}^{V_N} \left| \frac{\overline{I_{\text{central\_in}}}(V_n - V_N/2)}{\overline{I_{\text{central\_ac}}}(V_n - V_N/2)} \right|}{N} \tag{3}$$

where V_{peak} is the potential corresponding to the current peak, V_N is the range of voltages around the peak that were included in the measurement, N is the number of samples, $\overline{I_{\text{central\_ac}}}$ and $\overline{I_{\text{central\_in}}}$ are the average of the 50 cycle current measurements of the central cell WEs when the cell is active and inactive

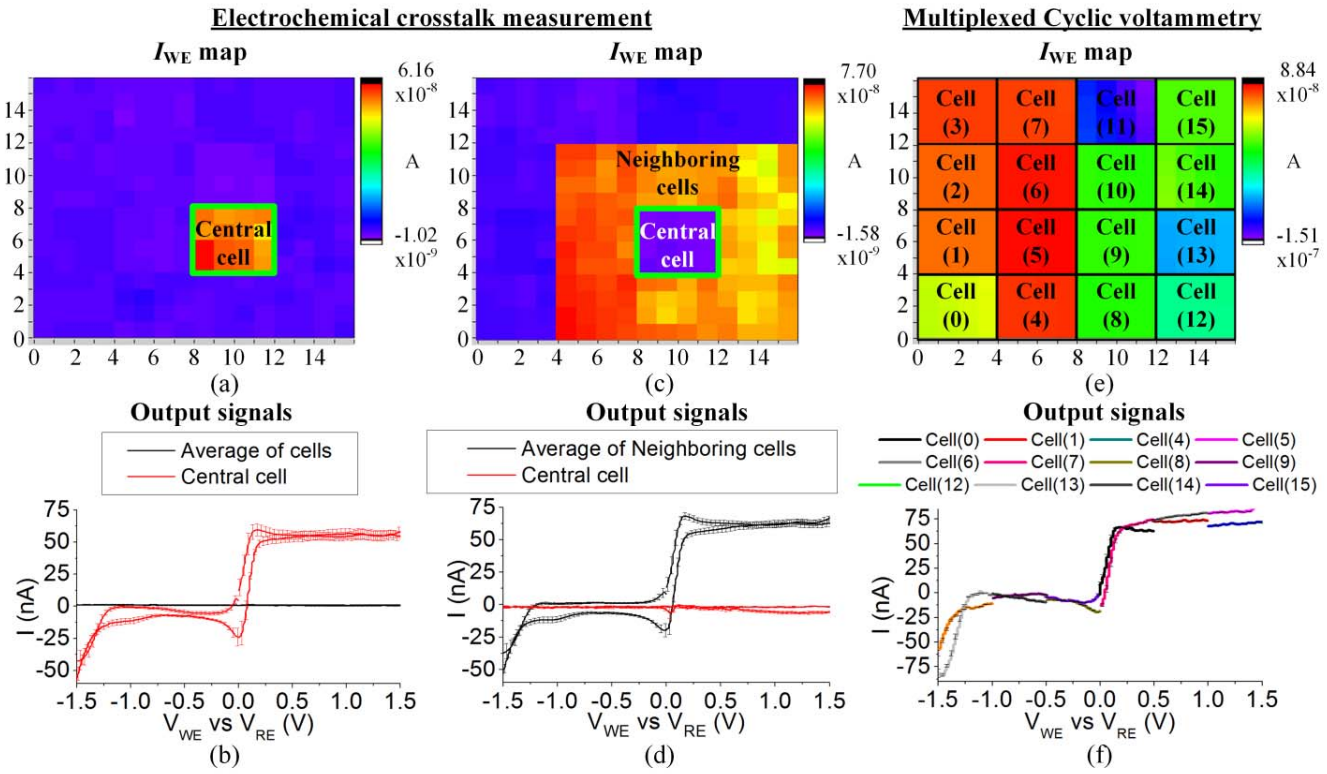

Fig. 10. (a) WE current map of the oxidation peak current and (b) the corresponding CV when the central cell (indicated in green) was active. (c) WE current map of the oxidation peak current and (d) the corresponding CV when the central cell was inactive. (e) WE current map at the beginning of the first cycle of a multiplexed CV and (f) the reconstructed CV of demultiplexed output signals averaged at each electrochemical cell.

respectively. The inter-cell electrochemical cross-talk was calculated around the current peaks, where it was observed to maximize, using $V_N = 100$ mV. An average value of 12.3 % was obtained, indicating a low leakage current owing to the use of our electrode and circuit design. This cross-talk value was obtained by excluding data values from $I_{central\_ac}$ and $I_{central\_in}$ that were lower than the noise floor. The noise floor was calculated by performing a third measurement with all cells at $V_{WE} - V_{RE} = 0$ V for the same duration as a 50 cycle CV and using NF $= \overline{\text{rms}(I_{cell\_noise}(i))} = 1.04$ nA, where i is the cell number and $I_{cell\_noise}(i)$ is the average current from the WEs of a cell. In addition to the NF, using the same data, the limit of detection (LOD) of the sensor was calculated using: LOD $= \mu_{\overline{I_{cell\_noise}(i)}} \pm 3.3 \times SD_{\overline{I_{cell\_noise}(i)}} =$ 880 ± 510 pA, where μ is the mean value and SD the standard deviation. The thermal noise for the 200 kΩ $R_{I\ to\ V}$ resistors is only 8 % of the LOD. The relatively high NF and LOD values are attributed to the accuracy of the PXI readout system with a minimum detectable voltage at 291 μV. Based on these measurements and the I_{max} value, the SNR and DR were calculated as 82.6 dB and 75.4 dB respectively.

B. Multiplexed Cyclic Voltammetry

Using the capability of independently operated electrochemical sensors, one-pot chemical and biological applications become possible. A demonstration of how the low cross-talk value of our single chamber ECM allows for independent potential scans with a low leakage current is illustrated by a novel electrochemical technique that we introduce. We call this technique multiplexed cyclic voltammetry and it increases the equivalent scan rate υ_{eq} by the use of our ECM features. The input waveform function of a CV was resolved over all the electrochemical cells by splitting it into independent (differential) input signals. Each portion of the waveform function was applied to a corresponding electrochemical cell. On every new cycle the waveform function portions were recycled consecutively. In Fig. 10(e) a WE current map at the beginning of the first cycle (after a pre-concentration cycle) is shown, using the sample solution that was used in the electrochemical cross-talk measurement. The current map demonstrates the redox responses to different concurrent waveform settings. Demultiplexing the averaged cell current outputs resulted in a reconstructed CV, shown in Fig. 10(f), results from cells 2, 3 and 10, 11 were excluded to show a range from −1.5 V to 1.5 V. The CV's behavior is similar to the response of a normal CV i.e. Fig. 10(b) and 10(d). The advantage of a multiplexed CV is an increase in the resulting equivalent scan rate, according to $\upsilon_{eq} = \upsilon_{cell} \times N_{cells}$, where υ_{cell} is the scan rate used at each electrochemical cell, and N_{cells} is the number of electrochemical cells. The CV of Fig. 10(f) has a $\upsilon_{eq} = 24$ V/s which is 12 times faster than a normal CV with $\upsilon_{cell} = 2$ V/s. Scaling up the array with more cells will lead to scan rates comparable to FSCV which suffers from the need to remove background current and also signal distortion caused by the Ohmic drop [46], [47]. Multiplexed cyclic voltammetry maintains the attractive reliable Faradaic current behavior of low scan rates and at the same time increases the temporal resolution. The increased equivalent

TABLE II
COMPARISON TABLE OF CMOS AMPEROMETRIC MEA SYSTEMS

Reference	**JSSC-08** [23]	**JMM-11** [53]	**Anal. Chem.-14** [22]	**TBioCAS-13** [44]	**This work**
Electrochemical system type	3-electrode SE[a]	3-electrode SE[a]	3-electrode SE[a]	2-electrode SE[a]	3-electrode FD[a]
Technology	0.25 µm	0.6 µm	0.35 µm	0.35 µm	0.35 µm
Power Supply Voltage	2.5 V	5 V	3.3 V	3.3 V	3.3 V
Die Size	5 x 3 mm^2	6.5 x 3 mm^2	7.5 x 4.8 mm^2	3.8 x 3.1 mm^2	3.79 x 3.79 mm^2
Chip Sensing Area	Not Available	~3 × 3 mm^2	3.2 × 3.2 mm^2	3.15 × 1.9 mm^2	1.81 × 1.81 mm^2
WE size	70 × 70 μm^2 to 100 × 100 μm^2	ø 10 -100 μm^2	ø 25 μm^2 and ø 5 μm^2-50 μm^2	100 µm long bumps	20 × 20 μm^2
WE pitch	Not Available	100 µm	100 µm	200 µm	114 µm
Number of WEs	4 × 4 (16)	24 × 24 (576)	32 × 32 (1024)	16 × 12 (192)	16 × 16 (256)
WEs per readout Channel	1	24	16	1	16
Number of Potentiostats	4	1 (external)	1 (bipotentiostat)	192 (current conveyor)	16
Number of independent E-cells	1	1	1	4 × 24[b]	16
I_{max}	150 nA	5 µA	2 µA or 10 µA	350 nA	13 µA
Limit of Detection (LOD)	550 pA_{rms}	500 pA	100 pA or 1 nA	24 pA	1.39 nA
Readout SNR | Noise Floor	~55 dB @ 40 nA | Not Available	Not Available	73.6 dB @ 1 µA / channel | 540 fA_{rms} to 250 pA_{rms}	70.2 dB @ 300 nA / channel | Not Available	82.6 dB @ 13 µA / channel | 1.04 nA_{rms}
Cross-talk	Not Available	Not Available	Not Available	Not Available	12.3 %
Voltage Swing (V_{WE} vs V_{RE})	1.25 V_{pp} (used)	4 V_{pp}	2.8 V_{pp}	2 V_{pp} (simulated)	5.2 V_{pp}
Slew Rate	Not Available	Not Available	0.35 V/µs	13 V/µs	1.09 V/µs
Bandwidth	10 kHz	4 kHz	up to 1 kHz	1 kHz	150 kHz
Max. Sampling Rate	2.5 kS/s/channel	Not Available	1.4 MS/s/channel	1 kS/s	1.25 MS/s/channel
Max. Power dissipation	Not Available	25 ± 5 mW	Not Available	188 µW/channel (36 mW)	125.4 mW

[a]SE stands for single-ended potentiostat and FD stands for fully differential potentiostat.[b]A WE potential setting per 24 current conveyors.

scan rate makes it possible for the study of phenomena such as short-lived intermediate compound analysis in dye-sensitized solar cells [48] that currently only FSCV and amperometry are capable of monitoring.

VII. COMPARISON WITH THE STATE OF THE ART

The main specifications of this work are summarized and compared to prior MEA work in Table II. The presented system offers a high number of independently controlled electrochemical cells which can be compared to [44]. However, in that work a 2-electrode system with less control over the potential was used and the independent potential settings were not demonstrated. By using fully differential potentiostats the ECM benefited from the dual advantage of individual electrochemical cell control and a large (5.2 V_{pp}) potential scan range. Whilst the power consumption for the new chip is higher than previous designs, the chip operates at a far higher bandwidth, required for methods such as FSCV. Our system has a high maximum detectable current (I_{max}) not only for analyte detection but also for functionalization processes with the internal circuits. A high SNR was achieved with this feature. Conversely, a moderate LOD value was measured. However, when ferrocene is used as a redox label in DNA sensing, the "target" DNA strand places that redox label in very close proximity to the WE hence it can be used with CMOS MEAs [23]. FSCV can then be used to induce a redox current that can be estimated by $I_{peak} = n^2F^2\upsilon AD/4RTN_A$ [23], where I_{peak} is the peak current, n is the number of exchanged electrons, D is the coverage density and N_A is Avogadro's number. For DNA detection using ferrocene with at least a $D = 3 \times 10^{12}$ cm^{-2} and using a scan rate higher than $\upsilon = 400$ V/s the expected current would be at least 7.5 nA. This is considerably greater than the LOD = 1.39 nA achieved in this work, hence a signal would be detected. For other applications that are performed at high temperatures or have a higher sensitivity requirement other current conversion methods can be used in those cases to improve the system's performance and LOD [45].

The electrochemical cross-talk that was measured in this work is a combination of both electrical and chemical cross-talk. Such a figure of merit has not been reported before as this is the first time a multiple electrochemical cell system was investigated. To reduce the chemical cross-talk the WE pitch used in this work was kept larger than the one reported in the introduction [14] to ensure a good intra-cell isolation. The simulations presented in Section II show how the design of the electrode layout used in this work led to less electrical cross-talk in the array. Using this design we have shown that neighboring cells in an array can be operated at different electric potentials with negligible effects on each other's performance.

VIII. CONCLUSION

We have demonstrated a CMOS microelectrode array comprising independent electrochemical cells operating simultaneously in a single fluidic container. The array is made of biocompatible sites for electrochemistry with a suitable sensitivity. Owing to its wide bandwidth, high speed experiments can be performed. Its low cross-talk figure allows for parallel measurements and new techniques to be incorporated, making use of this system's features. Individual electrochemical cells each have their own on-chip electronic circuits forming self-regulating equipotential regions that surrounded their respective group of microelectrodes. The architecture takes advantage of a coaxial microelectrode geometry and a fully differential design that resulted in independent electrochemical measurements. An electrochemical cell-to-cell cross-

talk of only 12.3 % was recorded. As a consequence the electrochemical cells were used independently to perform a new technique that measures a CV more quickly using parallelization. Furthermore, the chip enables a range of different experiments to be carried out simultaneously. These include chronoamperometry and differential pulse voltammetry. The demonstrated electrode system can be scaled up to larger arrays with more electrochemical cells. As the measurements indicate, the ECM is suitable for use as a DNA microarray with several redox labels analyzed with FSCV using electrochemical cells operating in different potential windows. In conventional systems the diffusion of redox labels and cross-hybridization of DNA "targets" to neighboring electrodes is a source of chemical cross-talk [23], [26], [49]. Our system minimizes the diffusion and improves the selectivity by limiting the detection of each analyte to its respective cell. A future chip could integrate a greater number of electrochemical cells on CMOS and provide the architecture for a sensor system-on-chip complete with a microprocessor, data acquisition, and wireless technology. Such integration could lead to a portable self-contained lab-on-a-chip for environmental and biomedical simultaneous multiple analyte sensing applications.

ACKNOWLEDGMENT

The authors of this document would like to hereby thank Mr. James Beeley for his input in the digital ASIC design, Prof. Leroy Cronin for valuable discussions, Dr. Corrie Farmer for his valuable input in fabrication and all the staff of the James Watt Nanofabrication Centre (JWNC) for their contribution. All our datasets can be accessed here: http://dx.doi.org/10.5525/gla.researchdata.437.

REFERENCES

[1] A. Volta and J. Banks, "I. On the electricity excited by the mere contact of conducting substances of different kinds," *Philos. Mag.*, vol. 7, no. 28, pp. 289–311, Sep. 1800.

[2] A. J. Bard, Ed., *Encyclopedia of Electrochemistry*. Weinheim, Germany: Wiley, 2007.

[3] E.-H. Yoo and S.-Y. Lee, "Glucose biosensors: An overview of use in clinical practice," *Sensors*, vol. 10, no. 5, pp. 4558–4576, May 2010.

[4] C. O. Park, J. W. Fergus, N. Miura, J. Park, and A. Choi, "Solid-state electrochemical gas sensors," *Ionics*, vol. 15, no. 3, pp. 261–284, 2009.

[5] T. Flores, G. Goetz, X. Lei, and D. Palanker, "Optimization of return electrodes in neurostimulating arrays," *J. Neural Eng.*, vol. 13, no. 3, p. 036010, Jun. 2016.

[6] M. E. Spira and A. Hai, "Multi-electrode array technologies for neuroscience and cardiology," *Nature Nanotechnol.*, vol. 8, no. 2, pp. 83–94, Feb. 2013.

[7] O. Ordeig, J. del Campo, F. X. Munoz, C. E. Banks, and R. G. Compton, "Electroanalysis utilizing amperometric microdisk electrode arrays," *Electroanalysis*, vol. 19, nos. 19–20, pp. 1973–1986, Oct. 2007.

[8] H. Li, X. Liu, L. Li, X. Mu, R. Genov, and A. Mason, "CMOS electrochemical instrumentation for biosensor microsystems: A review," *Sensors*, vol. 17, no. 1, p. 74, Dec. 2016.

[9] I. L. Jones, P. Livi, M. K. Lewandowska, M. Fiscella, B. Roscic, and A. Hierlemann, "The potential of microelectrode arrays and microelectronics for biomedical research and diagnostics," *Anal. Bioanal. Chem.*, vol. 399, no. 7, pp. 2313–2329, Mar. 2011.

[10] W. Maly, "Cost of silicon viewed from VLSI design perspective," in *Proc. 31st Annu. Conf. Design Autom. Conf. (DAC)*, 1994, pp. 135–142.

[11] A. Bard and L. Faulkner, *Electrochemical Methods: Fundamentals and Applications*. Hoboken, NJ, USA: Wiley, 2001.

[12] N. H. Lovell, S. Dokos, E. Cheng, and G. J. Suaning, "Simulation of parallel current injection for use in a vision prosthesis," in *Proc. Conf. 2nd Int. IEEE EMBS Conf. Neural Eng.*, Mar. 2005, pp. 458–461.

[13] G. K. Moghaddam, N. H. Lovell, R. G. H. Wilke, G. J. Suaning, and S. Dokos, "Performance optimization of current focusing and virtual electrode strategies in retinal implants," *Comput. Methods Programs Biomed.*, vol. 117, no. 2, pp. 334–342, 2014.

[14] B. Zhang, K. L. Adams, S. J. Luber, D. J. Eves, M. L. Heien, and A. G. Ewing, "Spatially and temporally resolved single-cell exocytosis utilizing individually addressable carbon microelectrode arrays," *Anal. Chem.*, vol. 80, no. 5, pp. 1394–1400, Mar. 2008.

[15] J. Guo and E. Lindner, "Cyclic voltammograms at coplanar and shallow recessed microdisk electrode arrays: Guidelines for design and experiment," *Anal. Chem.*, vol. 81, no. 1, pp. 130–138, Jan. 2009.

[16] T. Kuno, K. Niitsu, and K. Nakazato, "Amperometric electrochemical sensor array for on-chip simultaneous imaging," *Jpn. J. Appl. Phys.*, vol. 53, no. 4S, p. 04EL01, Jan. 2014.

[17] E. P. Anderson, J. S. Daniels, N. Pourmand, and T. H. Lee, "Crosstalk in integrated microarrays with current sensing," *IEEE Trans. Circuits Syst. I, Reg. Papers*, vol. 55, no. 11, pp. 3756–3762, Dec. 2008.

[18] P. Yu and G. S. Wilson, "An independently addressable microbiosensor array: What are the limits of sensing element density?" *Faraday Discussions*, vol. 116, pp. 305–317, Jun. 2000.

[19] D. C. Kirkpatrick, C. J. McKinney, P. B. Manis, and R. M. Wightman, "Expanding neurochemical investigations with multi-modal recording: Simultaneous fast-scan cyclic voltammetry, iontophoresis, and patch clamp measurements," *Analyst*, vol. 141, no. 16, pp. 4902–4911, 2016.

[20] M. P. Marsh, J. E. Koehne, R. J. Andrews, M. Meyyappan, K. E. Bennet, and K. H. Lee, "Carbon nanofiber multiplexed array and wireless instantaneous neurotransmitter concentration sensor for simultaneous detection of dissolved oxygen and dopamine," *Biomed. Eng. Lett.*, vol. 2, no. 4, pp. 271–277, Dec. 2012.

[21] M. K. Zachek, P. Takmakov, B. Moody, R. M. Wightman, and G. S. McCarty, "Simultaneous decoupled detection of dopamine and oxygen using pyrolyzed carbon microarrays and fast-scan cyclic voltammetry," *Anal. Chem.*, vol. 81, no. 15, pp. 6258–6265, Jun. 2009.

[22] J. Rothe, O. Frey, A. Stettler, Y. Chen, and A. Hierlemann, "Fully integrated CMOS microsystem for electrochemical measurements on 32×32 working electrodes at 90 frames per second," *Anal. Chem.*, vol. 86, no. 13, pp. 6425–6432, Jul. 2014.

[23] P. M. Levine, P. Gong, R. Levicky, and K. L. Shepard, "Active CMOS sensor array for electrochemical biomolecular detection," *IEEE J. Solid-State Circuits*, vol. 43, no. 8, pp. 1859–1871, Aug. 2008.

[24] S. M. Martin, F. H. Gebara, T. D. Strong, and R. B. Brown, "A fully differential potentiostat," *IEEE Sensors J.*, vol. 9, no. 2, pp. 135–142, Feb. 2009.

[25] K. Maurer *et al.*, "Electrochemically generated acid and its containment to 100 micron reaction areas for the production of DNA microarrays," *PLoS ONE*, vol. 1, no. 1, p. e34, Dec. 2006.

[26] P. M. Levine, P. Gong, R. Levicky, and K. L. Shepard, "Real-time, multiplexed electrochemical DNA detection using an active complementary metal-oxide-semiconductor biosensor array with integrated sensor electronics," *Biosensors Bioelectron.*, vol. 24, no. 7, pp. 1995–2001, Mar. 2009.

[27] N. Hüsken, M. Gębala, W. Schuhmann, and N. Metzler-Nolte, "A single-electrode, dual-potential ferrocene–PNA biosensor for the detection of DNA," *ChemBioChem*, vol. 11, no. 12, pp. 1754–1761, 2010.

[28] A. Hung, D. Zhou, R. Greenberg, and J. W. Judy, "Dynamic electrochemical simulation of micromachined electrodes for neural-stimulation systems," in *Proc. 1st Int. IEEE EMBS Conf. Neural Eng.*, Mar. 2003, pp. 200–203.

[29] B. A. Cales, R. G. Compton, J. P. Larsen, and R. A. Spackman, "Ohmic distortion of mass transport and of current–voltage curves at a channel electrode," *Electroanalysis*, vol. 8, no. 10, pp. 913–917, Oct. 1996.

[30] K. Gong, Q. Fang, S. Gu, S. F. Y. Li, and Y. Yan, "Nonaqueous redox-flow batteries: Organic solvents, supporting electrolytes, and redox pairs," *Energy Environ. Sci.*, vol. 8, no. 12, pp. 3515–3530, 2015.

[31] J. Bisquert, G. Garcia-Belmonte, F. Fabregat-Santiago, N. S. Ferriols, P. Bogdanoff, and E. C. Pereira, "Doubling exponent models for the analysis of porous film electrodes by impedance. Relaxation of TiO_2 nanoporous in aqueous solution," *J. Phys. Chem. B*, vol. 104, no. 10, pp. 2287–2298, 2000.

[32] J. E. B. Randles, "Kinetics of rapid electrode reactions," *Discussions Faraday Soc.*, vol. 1, p. 11, Mar. 1947.

[33] W. Franks, I. Schenker, P. Schmutz, and A. Hierlemann, "Impedance characterization and modeling of electrodes for biomedical applications," *IEEE Trans. Biomed. Eng.*, vol. 52, no. 7, pp. 1295–1302, Jul. 2005.

[34] D. Tang, J. Lu, L. Zhuang, and P. Liu, "Calculations of the exchange current density for hydrogen electrode reactions: A short review and a new equation," *J. Electroanal. Chem.*, vol. 644, no. 2, pp. 144–149, Jun. 2010.
[35] E. Laviron, "General expression of the linear potential sweep voltammogram in the case of diffusionless electrochemical systems," *J. Electroanal. Chem. Interfacial Electrochem.*, vol. 101, no. 1, pp. 19–28, Jul. 1979.
[36] D. Borkholder, "Cell based biosensors using microelectrodes," Stanford Univ., Stanford, CA, USA, Tech. Rep., 1998.
[37] Z. Stojek, "The electrical double layer and its structure," in *Electroanalytical Methods*. Berlin, Germany: Springer, 2010, pp. 3–9.
[38] N. Bako, Z. Butkovic, and A. Baric, "Design of fully differential folded cascode operational amplifier by the g_m/I_D methodology," in *Proc. 33rd Int. Convention*, May 2010, vol. 2. no. 9, pp. 89–94.
[39] R. Hintsche, J. Albers, H. Bernt, and A. Eder, "Multiplexing of microelectrode arrays in voltammetric measurements," *Electroanalysis*, vol. 12, no. 9, pp. 660–665, May 2000.
[40] R. Redd, M. Spak, J. Sagan, O. Lehar, and R. Dammel, "Lithographic process for high-resolution metal lift-off," *Proc. SPIE*, vol. 3678, pp. 641–651, Mar. 1999.
[41] J. A. Cunningham, "Expanded contacts and interconnexions to monolithic silicon integrated circuits," *Solid-State Electron.*, vol. 8, no. 9, pp. 735–738, Sep. 1965.
[42] B. C. Cheah *et al.*, "An integrated circuit for chip-based analysis of enzyme kinetics and metabolite quantification," *IEEE Trans. Biomed. Circuits Syst.*, vol. 10, no. 3, pp. 721–730, Jun. 2016.
[43] N. G. Tsierkezos and U. Ritter, "Electrochemical impedance spectroscopy and cyclic voltammetry of ferrocene in acetonitrile/acetone system," *J. Appl. Electrochem.*, vol. 40, no. 2, pp. 409–417, Feb. 2010.
[44] M. H. Nazari, H. Mazhab-Jafari, L. Leng, A. Guenther, and R. Genov, "CMOS neurotransmitter microarray: 96-Channel integrated potentiostat with on-die microsensors," *IEEE Trans. Biomed. Circuits Syst.*, vol. 7, no. 3, pp. 338–348, Jun. 2013.
[45] M. Crescentini, M. Bennati, M. Carminati, and M. Tartagni, "Noise limits of CMOS current interfaces for biosensors: A review," *IEEE Trans. Biomed. Circuits Syst.*, vol. 8, no. 2, pp. 278–292, Apr. 2014.
[46] D. L. Robinson, A. Hermans, A. T. Seipel, and R. M. Wightman, "Monitoring rapid chemical communication in the brain," *Chem. Rev.*, vol. 108, no. 7, pp. 2554–2584, Jul. 2008.
[47] D. O. Wipf, E. W. Kristensen, M. R. Deakin, and R. M. Wightman, "Fast-scan cyclic voltammetry as a method to measure rapid heterogeneous electron-transfer kinetics," *Anal. Chem.*, vol. 60, no. 4, pp. 306–310, Feb. 1988.
[48] T. Daeneke, T.-H. Kwon, A. B. Holmes, N. W. Duffy, U. Bach, and L. Spiccia, "High-efficiency dye-sensitized solar cells with ferrocene-based electrolytes," *Nature Chem.*, vol. 3, no. 3, pp. 213–217, Mar. 2011.
[49] X. Feng *et al.*, "Ratiometric biosensor array for multiplexed detection of microRNAs based on electrochemiluminescence coupled with cyclic voltammetry," *Biosensors Bioelectron.*, vol. 75, pp. 308–314, Jan. 2016.
[50] G. Zotti, G. Schiavon, S. Zecchin, and D. Favretto, "Dioxygen-decomposition of ferrocenium molecules in acetonitrile: The nature of the electrode-fouling films during ferrocene electrochemistry," *J. Electroanal. Chem.*, vol. 456, nos. 1–2, pp. 217–221, 1998.
[51] A. A. Maryott and E. R. Smith, *Table of Dielectric Constants of Pure Liquids*, vol. 514. National Bureau of Standards Circular, 1951.
[52] A. M. Bond, K. B. Oldham, and G. A. Snook, "Use of the ferrocene oxidation process to provide both reference electrode potential calibration and a simple measurement (via semiintegration) of the uncompensated resistance in cyclic voltammetric studies in high-resistance organic solvents," *Anal. Chem.*, vol. 72, no. 15, pp. 3492–3496, Aug. 2000.
[53] J. Rothe, M. K. Lewandowska, F. Heer, O. Frey, and A. Hierlemann, "Multi-target electrochemical biosensing enabled by integrated CMOS electronics," *J. Micromech. Microeng.*, vol. 21, no. 5, p. 054010, 2011.

Christos Giagkoulovits (S'16) received the B.Sc. degree in physics and the M.Sc. degree in electronics and communications (radioelectronics) from the University of Patras, Patras, Greece, in 2011 and 2013, respectively. He is currently pursuing the Ph.D. degree in electrical and electronic engineering with the Microsystems Technology Group, University of Glasgow. His research interests include mixed-mode CMOS integrated circuits for biomedical applications, low cost and low power biological sensors, sensor arrays, and microsystems for sustainable lifestyle applications.

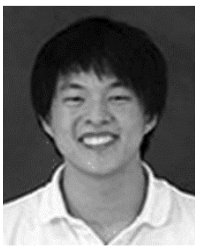

Boon Chong Cheah received the B.Eng. degree in electronic and electrical engineering and the M.Sc. (Eng.) degree in nanotechnology and advanced electronic devices from the University of Leeds, Leeds, U.K., in 2010 and 2011 respectively, and the Ph.D. degree in electronics and electrical engineering from the University of Glasgow in 2017 that was funded by the Lord Kelvin Adam Smith Scholarship.

He was with Intel Corporation in 2012. He is currently a Research Assistant with the Microsystem Technology Group. His research interests include nanofabrication, biochemical sensors, sensor systems, CMOS electronics, biochemistry, and printing techniques.

Mohammed A. Al-Rawhani received the B.Sc. degree in electronics and telecommunication engineering from Al-Ahliyya Amman University, Amman, Jordan, in 2004, and the M.Sc. degree in electrical and electronic engineering and the Ph.D. degree in electronic integration design for biomedical applications from the University of Glasgow, Glasgow, U.K., in 2007 and 2012, respectively. His research interests include CMOS low- and high-voltage analogue/mixed-signal integrated circuits and front-ends for optical sensing biomedical applications.

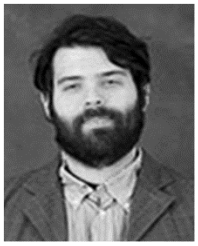

Claudio Accarino received the M.Sc. degree in biomedical engineering from the University of Strathclyde, Glasgow, U.K., in 2014, where he is currently pursuing the Ph.D. degree on integrative sensing and measurements with the Microsystem Technology Group and the Centre for Doctoral Training in Integrative Sensing and Measurements. His research interests include CMOS electronics, optoelectronics, and low-illumination imaging.

Christoph Busche received the Dr.rer.nat. degree in inorganic chemistry from the Ruprecht-Karls-Universität Heidelberg, Germany, in 2009, with a focus on molecular magnetism of Bispidine coordination compounds. From 2010 to 2015, he was a Post-Doctoral Research Assistant with the School of Chemistry, University of Glasgow, U.K. In 2015, he received a personal research fellowship from the Royal Society of Edinburgh/Scottish Government and is currently involved in the topic of molecular electronics at the University of Glasgow, U.K.

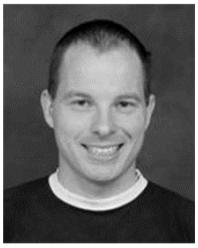

James P. Grant received the B.Sc. and Ph.D. degrees in physics from the University of Glasgow, Glasgow, U.K., in 2002 and 2006, respectively. He is currently a Post-Doctoral Research Fellow with the School of Engineering, University of Glasgow. His research interests include nanofabrication, metamaterial devices, plasmonics, terahertz systems, sensors, imaging, and CMOS electronics.

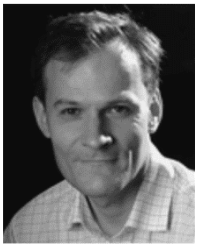

David R. S. Cumming (M'97–SM'08–F'13) received the B.Eng. degree in electronic and electrical engineering from the University of Glasgow, Glasgow, U.K., in 1989, and the Ph.D. degree from the University of Cambridge, Cambridge, U.K., in 1993. He currently leads the Microsystem Technology Group, School of Engineering, University of Glasgow, where he is also the Head of Engineering. His research on CMOS ion sensitive array technology has also been commercialized into the ion torrent next-generation sequencing system. He is a Fellow of the Royal Society of Edinburgh. He was a recipient of the Royal Society Wolfson Merit Award.